

## Roles of breaking waves and Langmuir circulation in the surface boundary layer of a coastal ocean

Shuang Li,<sup>1</sup> Ming Li,<sup>2</sup> Gregory P. Gerbi,<sup>3</sup> and Jin-Bao Song<sup>4</sup>

Received 8 February 2013; revised 29 August 2013; accepted 30 August 2013; published 8 October 2013.

[1] Breaking waves and Langmuir circulation are two important turbulent processes in the wind-driven upper ocean. To investigate their roles in generating turbulence in the surface boundary layer of a coastal ocean, a large eddy simulation model is used to simulate the turbulence measurements collected at the Martha's Vineyard Coastal Observatory's Air-Sea Interaction Tower, during the Coupled Boundary Layers and Air-Sea Transfer (CBLAST) experiment in 2003. The model provides reasonable predictions for the vertical profiles of vertical velocity variance, turbulent kinetic energy (TKE), energy dissipation rates, and heat flux. It shows breaking waves dominating turbulence generation near the ocean surface and turbulent large eddies characteristic of Langmuir circulation deeper in the water column. Diagnostic analysis of TKE budget in the model shows a dominant balance between turbulent transport and dissipation near the surface and a dominant balance between shear production and dissipation at deeper depths. Although the Stokes production is a significant term in the TKE budget balance near the surface, it is smaller than shear production. The turbulent transport is large in the near-surface zone and is still significant in the region affected by Langmuir circulation. These results are in agreement with a conclusion inferred from a recent analysis of the near-surface turbulence measurements at the CBLAST site.

**Citation:** Li, S., M. Li, G. P. Gerbi, and J.-B. Song (2013), Roles of breaking waves and Langmuir circulation in the surface boundary layer of a coastal ocean, *J. Geophys. Res. Oceans*, 118, 5173–5187, doi:10.1002/jgrc.20387.

### 1. Introduction

[2] Surface waves affect turbulence in the wind-driven ocean surface boundary layer mainly in two ways: (1) breaking waves inject turbulent kinetic energy (TKE) at the ocean surface; (2) the interaction of wave-induced Stokes drift current and mean wind-driven current [Craig and Leibovich, 1976] or preexisting turbulence [Teixeira and Belcher, 2002] generates counter-rotating vortices known as Langmuir circulation or Langmuir turbulence. Dissipation rates of TKE associated with wave breaking are found to be one to two orders of magnitude larger than those expected in turbulence near a rigid boundary [Agrawal *et al.*, 1992; Craig and Banner, 1994; Terray *et al.*, 1996]. Langmuir circulation produces vertical velocity variance 2–3 times larger than that from shear turbulence [McWilliams *et al.*, 1997; D'Asaro, 2001; Tseng and D'Asaro,

2004; Li *et al.*, 2005; Kukulka *et al.*, 2009]. Despite these investigations, the roles of wave breaking and Stokes drift in setting turbulence characteristics in the ocean surface layer remain unclear.

[3] The Coupled Boundary Layer and Air-Sea Transfer (CBLAST) program sponsored by U.S. Office of Naval Research was designed to investigate the air-sea interaction and coupling between the atmospheric and oceanic boundary layers across the wavy ocean surface. As part of the CBLAST program [see Edson *et al.*, 2007; Black *et al.*, 2007; Chen *et al.*, 2007 for reviews], extensive observations were made using instruments deployed in the ocean and atmosphere at the Martha's Vineyard Coastal Observatory's (MVCO) Air-Sea Interaction Tower (ASIT), located in 16 m of water on the New England shelf. The turbulence measurements collected during CBLAST offer an excellent opportunity to investigate how surface wave processes such as breaking waves and Langmuir circulation affect the ocean surface mixed layer.

[4] Using the turbulence measurements at ~2 m depth below the surface, Gerbi *et al.* [2009] investigated the energetics of turbulence. They estimated the Stokes production, buoyancy production, and dissipation terms and placed an upper bound on the shear production. Since the pressure work and transport terms were difficult to estimate from observations, they inferred the total transport term from a consideration of the TKE budget balance and estimate of time-tendency term. Gerbi *et al.* [2009] found that the Stokes production and buoyancy production were 2–3

<sup>1</sup>Ocean College, Zhejiang University, Hangzhou, China.

<sup>2</sup>Horn Point Lab, University of Maryland Center for Environmental Science, Cambridge, Maryland, USA.

<sup>3</sup>Physics and Geosciences Departments, Skidmore College, Saratoga Springs, New York, USA.

<sup>4</sup>Institute of Oceanology, Chinese Academy of Sciences, Qingdao, China.

Corresponding author: M. Li, Horn Point Lab., University of Maryland Center for Environmental Science, 2020 Horn Point Road, Cambridge, MD 21613, USA. (mingli@umces.edu)

orders of magnitude smaller than the dissipation, while the upper bound of shear production was 1 order magnitude smaller than the dissipation. This suggested that at depths around 2 m, the dissipation of TKE was primarily balanced by the divergence of TKE transport from breaking waves, consistent with previous modeling studies [Craig and Banner, 1994; Craig, 1996; Burchard, 2001]. Gerbi *et al.* [2009] interpreted this to mean that breaking waves were more important than Langmuir circulation in the turbulence generation. In a recent study, Kukulka *et al.* [2011, 2012] investigated turbulence characteristics at middepths in the CBLAST site and attributed the streaky structures observed on acoustic Doppler current profilers (ADCP) to Langmuir circulation. They also found that in large eddy simulations including Langmuir circulation, transport divergence is an important term in the TKE budget. However, their Large Eddy Simulation (LES) model did not consider the effects of breaking waves.

[5] There have been other interesting observational and modeling investigations of Langmuir circulation in shallow coastal oceans [Gargett *et al.*, 2004; Gargett and Wells, 2007; Tejada-Martinez and Grosch, 2007]. Field observations on the shallow shelf off New Jersey led to the discovery of Langmuir circulation extending throughout most of the water column under strong wind and wave forcing conditions. Such Langmuir circulations, reaching to the bottom boundary layer, have been termed supercells because of their profound influence on sediment resuspension and transport [Gargett *et al.*, 2004].

[6] Due to limited wind fetch and shallow water depth, air-sea interaction in coastal oceans is very different from that in the open ocean. First, surface waves in coastal oceans often have a sea state far from the fully developed sea. The drag coefficient is a strong function of wave age [Donelan *et al.*, 1993; Garrett, 1997]. At the same wind speed, the air-sea momentum flux in growing seas may be significantly larger than that in fully developed seas. The wave spectrum in growing seas is narrowly peaked, which affects the Stokes drift profile. In addition to locally generated waves, swell generated by remote storms can propagate to coastal oceans and be a substantial part of local wave fields. Langmuir circulation in a coastal ocean is more complex than that in the open ocean, because wind and wave conditions are highly variable and a range of sea state conditions are encountered [Churchill *et al.*, 2006]. It is challenging to quantify the effects of the complex sea state on the upper-ocean turbulence. However, Belcher *et al.* [2012] found that the turbulent Langmuir number  $La_t$  and the ratio of the mixed-layer depth to the Langmuir stability length provide a good description of upper-ocean turbulent flows in global oceans. They used reanalysis data to calculate global distributions of  $La_t$  and found that it is narrowly peaked around 0.3 in the open ocean but is broadly distributed between 0.2 and 0.8 in coastal oceans such as the Baltic Sea. Second, the presence of a frictional bed generates a bottom boundary layer, which may interact with the surface boundary layer in shallow water. The tidally driven bottom boundary layer ejects fluid parcels or boils to the surface boundary layer and may disrupt Langmuir circulation [Nimmo-Smith *et al.*, 1999; Thorpe, 2004]. Another mechanism of the tidal influence is due to mean

crosswind shear, which can distort and destroy Langmuir cells in a coastal ocean [Kukulka *et al.*, 2011].

[7] Many previous LES investigations of wind-driven upper ocean were limited to studies of Langmuir circulation under idealized and steady atmospheric forcing conditions [e.g., Skyllingstad and Denbo, 1995; McWilliams *et al.*, 1997; Min and Noh, 2004; Li *et al.*, 2005; Grant and Belcher, 2009; Noh *et al.*, 2011; McWilliams *et al.*, 2012]. Recently, LES studies have focused more on realistic hind-cast simulations and comparison against observations [Gargett and Wells, 2007; Tejada-Martinez and Grosch, 2007; Li *et al.*, 2009; Kukulka *et al.* 2009, 2010, 2012; Sullivan *et al.*, 2012]. A few LES studies have also considered the effects of breaking waves. Noh *et al.* [2004] added random forcing in the momentum equation of the LES model and effectively imposed a surface energy flux similar to that prescribed in the turbulence closure model of Craig and Banner [1994]. Based on field [Melville and Matusov, 2002] and laboratory [Melville *et al.*, 2002] observation of breaking waves, Sullivan *et al.* [2007] developed a stochastic representation of momentum impulses and energy fluxes in a field of breaking waves. They found that Langmuir circulation combines with breaking waves to increase turbulent energy and dissipation rate in the ocean mixed layer.

[8] This paper is an extension of Kukulka *et al.*'s [2012] LES simulation of the CBLAST observations by incorporating the effects of wave breaking. We examine the roles of breaking waves and Langmuir circulation in generating turbulence in the ocean surface boundary layer at the CBLAST experiment site on the shallow New England shelf. We also make a direct comparison of vertical velocity variance, TKE, turbulent fluxes and dissipation rate between the LES model results, and the measurements collected during CBLAST. The outline of this paper is as follows: Section 2 describes the model formulation and configuration. Section 3 reports the LES results and their comparison with the observations. In section 4, we study the TKE budget and evaluate the roles of breaking waves and Langmuir circulation in generating and modifying turbulence. Concluding remarks are made in section 5.

## 2. Model Configuration

[9] To simulate the CBLAST observations, we used the LES model that was first developed by Skyllingstad and Denbo [1995] and later extended for various surface boundary layer simulations [e.g., Skyllingstad *et al.*, 1999, 2000; Smyth *et al.*, 2002; Li *et al.*, 2005, 2009]. The LES model is based upon a filtering of the fluid equations of motion given by:

$$\begin{aligned} \frac{\partial u_i}{\partial t} + (u_j + u_{sj}) \frac{\partial u_i}{\partial x_j} + \varepsilon_{ijk} f_j (u_k + u_{sk}) \\ = -\frac{1}{\rho_0} \frac{\partial \pi}{\partial x_i} - g_i \frac{\rho}{\rho_0} + \varepsilon_{ijk} u_{sj} \omega_k + F_i + SGS, \end{aligned} \quad (1)$$

$$\frac{\partial \theta}{\partial t} + (u_j + u_{sj}) \frac{\partial \theta}{\partial x_j} = SGS, \quad (2)$$

$$\frac{\partial S}{\partial t} + (u_j + u_{sj}) \frac{\partial S}{\partial x_j} = SGS, \quad (3)$$

$$\frac{\partial u_i}{\partial x_i} = 0. \quad (4)$$

$$C_d = \frac{\kappa^2}{\left[\log \frac{\Delta z/2}{z_0}\right]^2} \quad (9)$$

where  $f$  is the Coriolis parameter,  $u$  is velocity,  $\omega$  is vorticity,  $\theta$  is temperature,  $S$  is salinity,  $u_s$  is the Stokes drift associated with surface waves,  $\pi$  is the modified pressure,  $g$  is the gravitational constant, and  $F_i$  is random forcing representing the generation of small-scale turbulence by wave breaking [Noh *et al.*, 2004]. These equations include the augmentation of LES equations by a Craik-Leibovich vortex force and an additional advection of any material property  $P$  by the wave-induced Lagrangian motion [McWilliams *et al.*, 1997]. The subgrid-scale terms shown schematically as SGS in equations (1)–(3) are calculated using the subgrid closure scheme provided by the filtered structure function (FSF) approach of Ducros *et al.* [1996].

[10] To represent the effects of wave breaking, we adopted the approach of Noh *et al.* [2004] by introducing small-scale random velocity fluctuations at the sea surface, with the integral length and time scales  $l_0$  and  $t_0$  corresponding to those of the near-surface small-scale turbulence generated by breaking waves,

$$F_1 = \frac{\alpha u_*}{t_0} \cos \gamma Ga(0; 1)(1 - \delta_{i3})\delta(z) \quad (5)$$

$$F_2 = \frac{\alpha u_*}{t_0} \sin \gamma Ga(0; 1)(1 - \delta_{i3})\delta(z) \quad (6)$$

where  $F_1$  and  $F_2$  represent the random forcing in the two horizontal directions ( $x$ ,  $y$ ),  $\alpha$  is a proportional constant,  $u_*$  is the surface friction velocity,  $\gamma$  is the angle of wind direction with respect to the  $x$  axis, and  $Ga(0; 1)$  is the Gaussian random function whose mean is 0 and variance is 1. The time scale of random forcing is given by  $t_0 = l_0/(\alpha u_*)$ . The rate of energy input by the random forcing,  $I$ , can be obtained from equation (1) by  $u_i(t)F_i(t)\Delta z$ , where  $\Delta z$  is the vertical grid size. Since the random forcing given at each time step is independent of the existing fluid field,  $I$  can be estimated as [Alvelius, 1999; Noh *et al.*, 2004]:

$$I = \frac{(\alpha u_*)^2}{4\sqrt{\pi}t_0} \Delta z = m u_*^3. \quad (7)$$

[11] Terray *et al.* [1996] analyzed turbulence measurements under conditions of strong wind forcing and suggested that breaking waves inject TKE down to a depth of about one significant wave height from the sea surface. Since the average significant wave height was about 0.5 m during the CBLAST experiment [Gerbi *et al.*, 2009], we chose  $l_0 = \Delta z = 0.5$  m. If the proportional coefficient  $\alpha = 8.92$  is selected, we obtain  $m = 100$ , which recovers the empirical value that Craig and Banner [1994] used in their parameterization of wave-breaking effects in turbulence closure models. In section 4.2, we examine the sensitivity of LES solutions to  $m$  values.

[12] At the bottom boundary, we employ a wall-layer model and specify a bottom stress using a drag law:

$$\frac{\tau}{\rho} = -\overline{u'w'} = C_d u |u|_{z=\Delta z/2} \quad (8)$$

where the drag coefficient is calculated from:

with  $z_0$  being the roughness height and  $\kappa = 0.4$  being the von Karman constant [Moeng *et al.*, 1984]. For a roughness height of  $z_0 = 1$  mm, the drag coefficient is  $C_d = 0.0052$  for the velocity at 0.25 m (1st grid) above the bottom boundary [He and Wilkin, 2006]. During the measurement period, stress and dissipation estimates near the bottom boundary were roughly consistent with a constant-stress logarithmic layer (J. Trowbridge, personal communication, 2011). Our bottom boundary condition is identical to the one used by Kukulka *et al.* [2012]. There are two approaches to model small-scale turbulence close to solid boundaries: (1) to resolve the near wall motion; (2) to use a wall-layer model. Tejada-Martinez and Grosch [2007] took the first approach, which has the advantage of directly simulating the near-wall flows but has the disadvantage that the computational cost increases with Reynolds number. We take the second approach in this paper. Piomelli and Balaras [2002] reviewed wall-layer models for LES simulations and concluded that the simple model based on the law-of-the-wall works well in flows over a flat boundary. This approach is not limited to moderate Reynolds number. However, Tejada-Martinez *et al.* [2012] found that the log layer near the bottom boundary is disrupted by Langmuir Circulation and could affect the interior flow. Their study, however, also indicates that for the parameters of our LES ( $La_t \sim 0.7$ ) disruption is unlikely to be significant.

[13] The CBLAST observations were made using instruments deployed at the Martha's Vineyard Coastal Observatory's (MVCO) Air-Sea Interaction Tower (ASIT). The tower on the New England Shelf is located about 3 km to the south of Martha's Vineyard and in water of about 16 m deep (Figure 1). Atmospheric measurements included velocity, temperature, humidity, and upwelling and downwelling short- and long-wave radiation [Edson *et al.*, 2007]. Bulk formulae [Fairall *et al.*, 2003] were used to estimate momentum flux and latent and sensible heat fluxes.

[14] Directional wave spectra  $G(\omega, \theta)$  were estimated from the ADCP measurements at the MVCO sea-node [Churchill *et al.*, 2006]. Following Gerbi *et al.* [2009], we can calculate the Stokes drift current in the two horizontal directions,

$$u_s(z) = \int_0^{2\pi} d\theta \cos \theta \int_0^\infty G(\omega, \theta) \omega k d\omega F_s, \quad (10)$$

$$v_s(z) = \int_0^{2\pi} d\theta \sin \theta \int_0^\infty G(\omega, \theta) \omega k d\omega F_s, \quad (11)$$

where

$$F_s = \frac{\cosh[2k(z+h)]}{\sinh^2(kh)}. \quad (12)$$

$$\omega^2 = gk \tanh(kh) \quad (13)$$

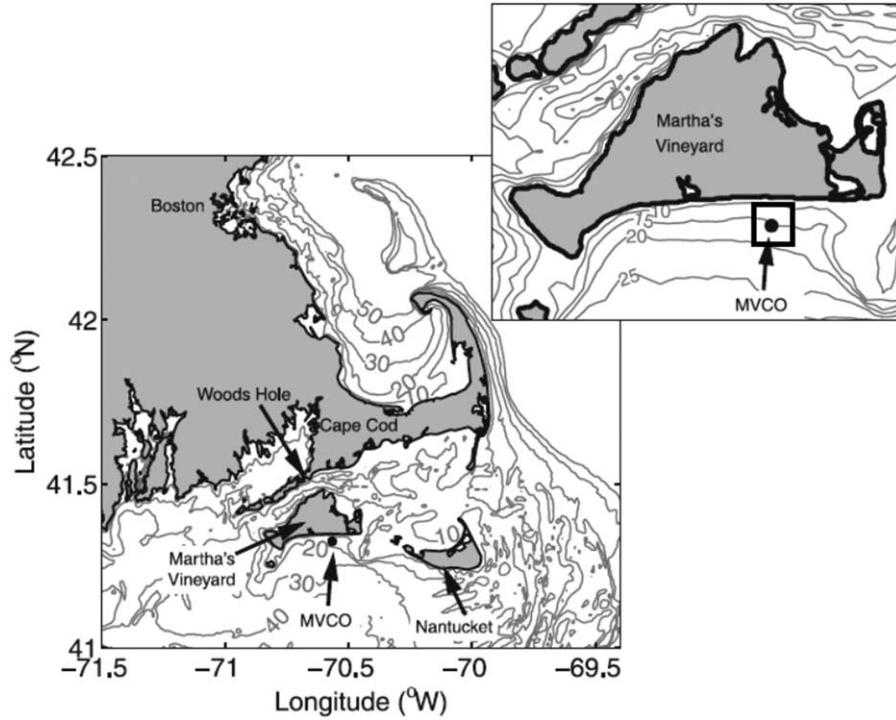


**Figure 1.** Maps showing the location of Martha Vineyard Coastal Observatory (MVCO). Contours show isobaths between 10 and 50 m. The inset map shows the area in the immediate vicinity of the CBLAST study site with the square box indicating the LES model domain (adapted from *Gerbi et al.* [2008]).

in which  $h$  is the water depth and  $k$  is the wavenumber. For waves in deep water ( $kh \gg 1$ ), equations (10) and (11) recover the classic Stokes drift formula derived by *Kenyon* [1969] and *Huang* [1971]. The directional wave spectrum can be separated into two components,

$$G(\omega, \theta) = D(\omega, \theta)S(\omega) \quad (14)$$

in which  $D(\omega, \theta)$  is the directional spreading function and  $S(\omega)$  is the one-dimensional wave height spectrum. As

noted by *Churchill et al.* [2006], reliable estimates of wave spectra were obtained only at wave frequencies lower than 0.4 Hz. At higher frequencies, we append the spectrum  $S(\omega)$  using a  $\omega^{-5}$  tail [*Banner*, 1990], as shown in Figure 2a. Figure 2b compares the surface Stokes drift current velocity ( $u_s, v_s$ ) calculated using the direct ADCP measurements and the corrected wave spectrum. Following *Kukulka et al.* [2012], we also calculated the Stokes drift by assuming a monochromatic surface wave with a significant wave height and wavelength consistent with

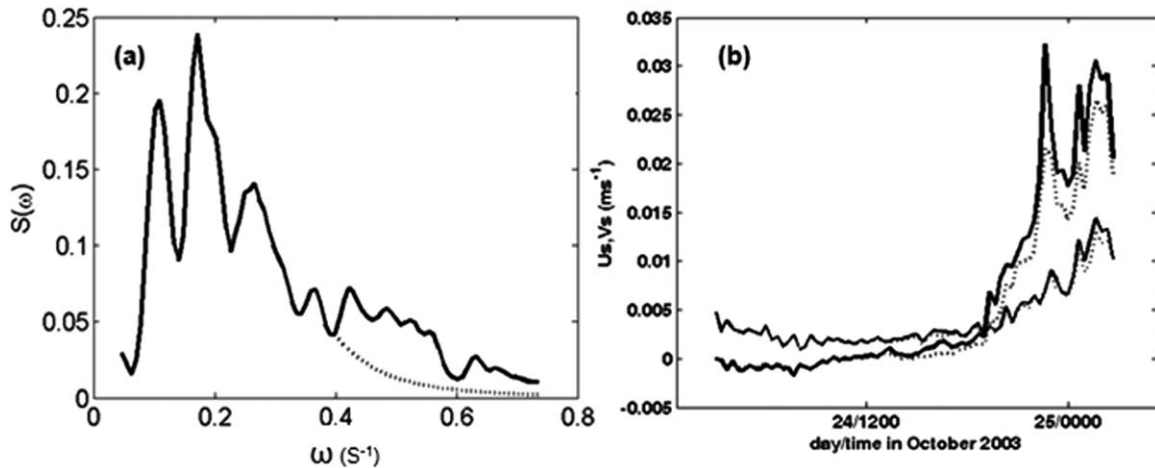


**Figure 2.** (a) Wave spectra (solid) obtained from 1200-kHz ADCP and the spectra (dashed) corrected at frequencies higher than 0.4 Hz. (b) Surface Stokes drift in the east-west direction (thick lines) and north-south direction (thin lines) obtained from the ADCP observations (dashed lines) and from the wave spectra corrected at high frequencies (solid lines).

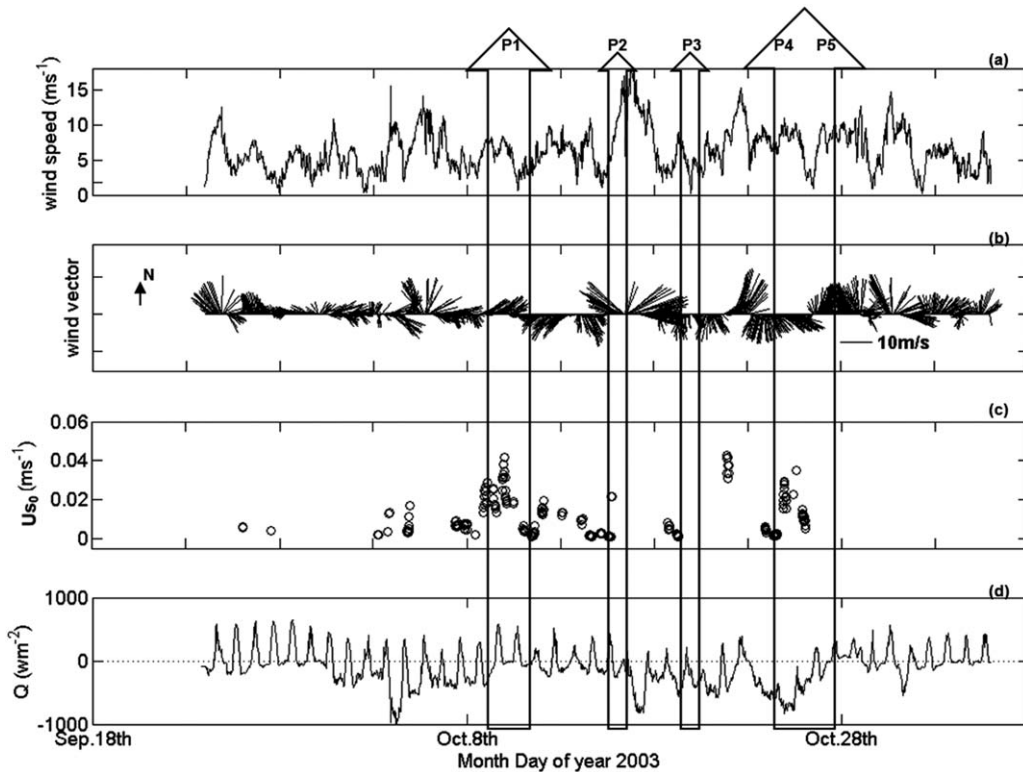


**Figure 3.** Time series of (a) wind-speed magnitude, (b) wind-speed vector, (c) surface Stokes drift, and (d) net surface heat flux for the duration of CBLAST experiments in 2003. P1–P5 represent five periods of LES simulations: P1 (19:00 7th to 19:00 9th October); P2 (8:50 13th to 22:10 13th October); P3 (11:50 17th to 2:50 18th October); P4 (3:50 to 8:50 23th October); and P5 (15:30 23th to 21:30 24th October).

observations. The two methods gave similar estimates for the Stokes drift current.

[15] We choose a LES model domain, which is centered at ASIT. The grid spacing is set to be 0.5 m in all three directions. The model has a horizontal dimension of  $160 \times 160$  m and a vertical depth of 16 m (a grid size of  $320 \times 320 \times 32$ ). We have also run the model in a smaller model domain of  $50 \times 50 \times 16$  m and found that the low-order turbulence statistics are insensitive to the domain size. The  $x$  axis is aligned with the east-west direction (positive for the eastward velocity) and the  $y$  axis with the north-south direction (positive for the northward velocity) (see Figure 1). The surface boundary conditions for the LES model include two horizontal wind stress components, net heat flux and latent heat flux. In the model, all incoming solar radiation is absorbed in the uppermost grid cell. The vertical profile of the Stokes drift current calculated above is supplied to the LES model. Periodic boundary conditions are imposed in the two horizontal directions. Tidal currents move in the along-shore direction and have the amplitude of  $\sim 0.3 \text{ m s}^{-1}$  and a dominant frequency at  $M_2$  [He and Wilkin, 2006; Kukulka et al., 2011]. Gerbi et al. [2009] observed that turbulence generated by the tidal currents was limited to the bottom few meters and did not affect turbulence dynamics in the surface mixed layer during the study periods. We did a test model run that included the tidal forcing via the prescription of an oscillating body force [e.g., Li et al. 2008, 2010] and found the same result.

[16] This paper focuses on the main CBLAST experiment conducted in 2003. Figure 3 provides a summary of the atmospheric forcing functions encountered during the fall when extensive measurements were made. Several wind events lasting a few days each passed through the experimental site. We have selected five events for detailed LES model simulations since they are representative of typical wind and sea state conditions observed during the CBLAST experiment. Moreover, data coverage and quality are best during these periods [Gerbi et al., 2008, 2009], thus allowing us to conduct direct model-data comparison. For each event, the LES model is initialized using observed profiles of temperature and salinity and zero currents.

[17] It should be noted that the turbulence Langmuir number  $La_t = \sqrt{u_*}/U_s$  [McWilliams et al., 1997] falls into a range between 0.5 and 0.8 for most of the wind events encountered during the CBLAST experiment, as shown in Figure 4d. Similar values of  $La_t$  were found by Kukulka et al. [2012]. These values are much larger than a typical value of 0.3 in fully developed seas in the open ocean [Li and Garrett, 1993; Belcher et al., 2012] but are similar to the values between 0.2 and 0.8 found in the Baltic Sea by Belcher et al. [2012]. Based on the LES simulations in the deep ocean, Li et al. [2005] found that upper-ocean turbulent flows are dominated by Langmuir circulation when  $La_t < 0.7$  and the normalized vertical turbulence intensity is a rapidly decreasing function of  $La_t$  for  $0.2 < La_t < 0.7$ . However, turbulence in the shallow coastal ocean is still

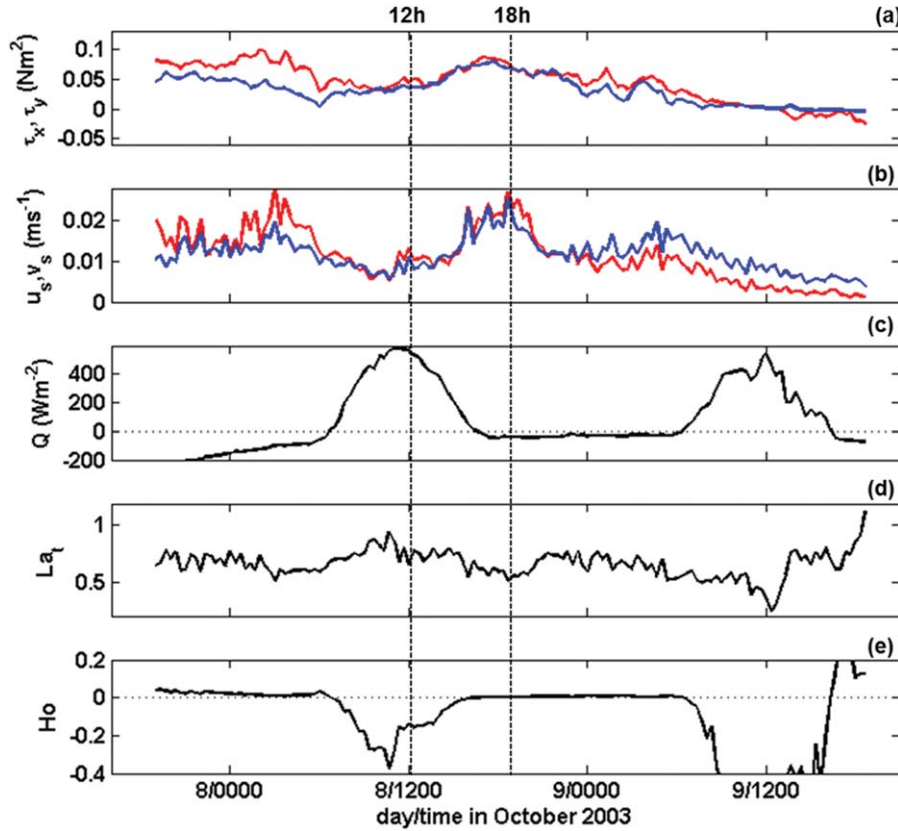


**Figure 4.** Time series of (a) wind stress and (b) surface Stokes drift in the east-west direction (red line, positive eastward) and north-south direction (blue line, positive northward), (c) net surface heat flux, (d) Turbulent Langmuir number  $La_t$ , and (e) Hoenikker number  $Ho$  during LES experiment P1, which began at 19:00 7th October (local time) and lasted for 48 h.

dominated by Langmuir circulation even when  $La_t > 0.7$  [Gargett and Wells, 2007; Kukulka et al. 2011, 2012], suggesting that the  $La_t$  threshold for the transition from the shear to Langmuir turbulence is larger in the shallow water.

### 3. Model Results and Comparison With Observations

[18] In this section, we present detailed LES simulation results of a selected event and show model-data comparisons of vertical turbulence velocity variance, TKE, energy dissipation rate, temperature difference, and heat flux obtained from all five events.

#### 3.1. Detailed Simulation Results for 1 Event (P1)

[19] Figure 4 shows the time series of atmospheric forcing at the CBLAST site over a 2 day period (8 and 9 October). The net surface flux  $Q$  exhibited a strong diurnal cycle: with a midday maximum of about  $578 \text{ Wm}^{-2}$  and slightly negative value (about  $-49 \text{ Wm}^{-2}$ ) during the night. Winds were predominantly westerly in the first 12 h but switched to southwesterly later on. The eastward wind stress showed two peaks of about  $0.1 \text{ Nm}^{-2}$  at local standard time (LST) 0400 and LST 1700, 8 October, and declined steadily in the following 24 hours. The northward wind stress steadily increased to a maximum of  $0.1 \text{ Nm}^{-2}$  at LST 1700, 8 October, but decreased thereafter, in sync

with the eastward component. The Stokes drift current reached its peak values at the two times when the wind stress peaked, although a smaller peak in the Stokes drift at LST 0400, 9 October, did not correspond to an increase in the wind stress and the waves may have been generated remotely and propagated onto the CBLAST site.

[20] Based on LES of steady wind and wave forcing in unstratified mixed-layer over a deep pycnocline, Li et al. [2005] constructed a regime diagram to distinguish different types of upper-ocean turbulent flows, including Langmuir turbulence, shear turbulence, and convective turbulence. The diagram is based on two dimensionless numbers: turbulent Langmuir number  $La_t$  and Hoenikker number  $Ho = 4B_0 / (U_s \beta u_*^2)$  [Li and Garrett, 1995] where  $U_s$  is the magnitude of the Stokes drift at the sea surface,  $1/\beta$  is the e-folding depth of the Stokes drift current, and  $B_0 = -\alpha g Q / (\rho_w C_p)$  is the surface buoyancy flux. Although the Stokes drift current in the shallow water has a vertical profile different from that in the deep ocean, we have calculated  $La_t$  and  $Ho$  to gauge the relative importance of wave forcing, buoyancy forcing, and shear stress. As shown in Figure 4d,  $La_t$  ranges between 0.5 and 0.8. According to Li et al. [2005] and other LES models in shallow water [Gargett and Wells, 2007; Kukulka et al., 2011, 2012], the turbulence during this period should have the characteristics of Langmuir turbulence.  $Ho$  is positive during the two nights but is of order  $O(10^{-2})$ , suggesting that

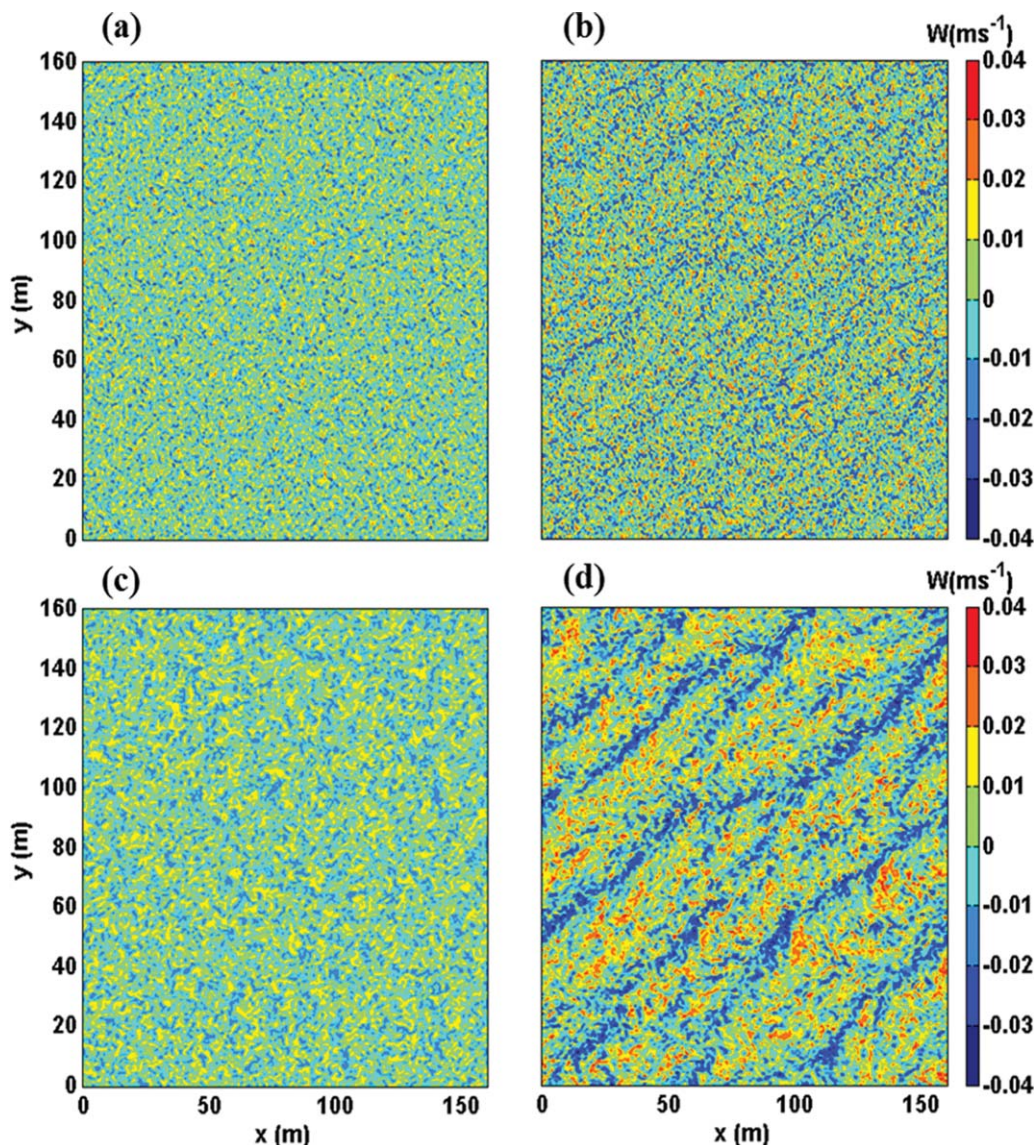


**Figure 5.** Horizontal distributions of vertical velocity (in unit of  $\text{ms}^{-1}$ ) at depths of 0.25 m (a/b) and 3.25 m (c/d) and at hour 12 (left column) and 18 (right column) during P1.

convective forcing is not a significant contributor in the turbulence generation (Figure 4e). On the other hand,  $Ho$  is more negative than  $-0.4$  during the daytime on October 8. It reached high negative values during the daytime on October 9 because the wind stress and the friction velocity were close to zero. In a recent paper, *Belcher et al.* [2012] constructed a new regime diagram to distinguish buoyancy-, wave-, and wind-driven turbulence in terms of dimensionless parameters  $La_t$  and  $h/L_L$  where  $h$  is the mixed-layer depth and  $L_L$  is the Langmuir stability length. The parameter  $h/L_L$  is of order  $O(10^{-2})$  during P1, suggesting that unstable buoyancy forcing is not the dominant contributor to turbulence generation.

[21] To examine how the upper ocean responded to the atmospheric forcing over the 2 day period, we have selected two time slices for detailed examinations of the three-dimensional turbulence fields: (1) LST 1200 on October 8 when the wind stress and Stokes drift were weak but surface heating was strongest; (2) LST 1800 on

October 8 when both the wind stress and Stokes drift current were strongest (see Figure 4). As shown in Figure 5, the vertical velocity distribution at the depth of 0.25 m shows small-scale random distributions representative of breaking waves. Although the random forcing  $F_i$  due to breaking waves is imposed only on the horizontal velocity fields, the vertical velocity fluctuations were generated near the surface boundary due to continuity. The breaking wave activities were stronger at hour 18 than at hour 12 because the wind stress was 2.7 times stronger. At the deeper depth (3.25 m), the flow patterns look very different between the two times: turbulent flows were weak and disorganized at hour 12. However, at hour 18, the flows organized into roughly seven parallel structures aligned with the wind direction.

[22] To further demonstrate the flow-pattern differences between the two time slices, we plot the horizontal distributions of east-west, north-south velocities and temperature at the 3.25 m depth (Figure 6). Under the low wind and wave

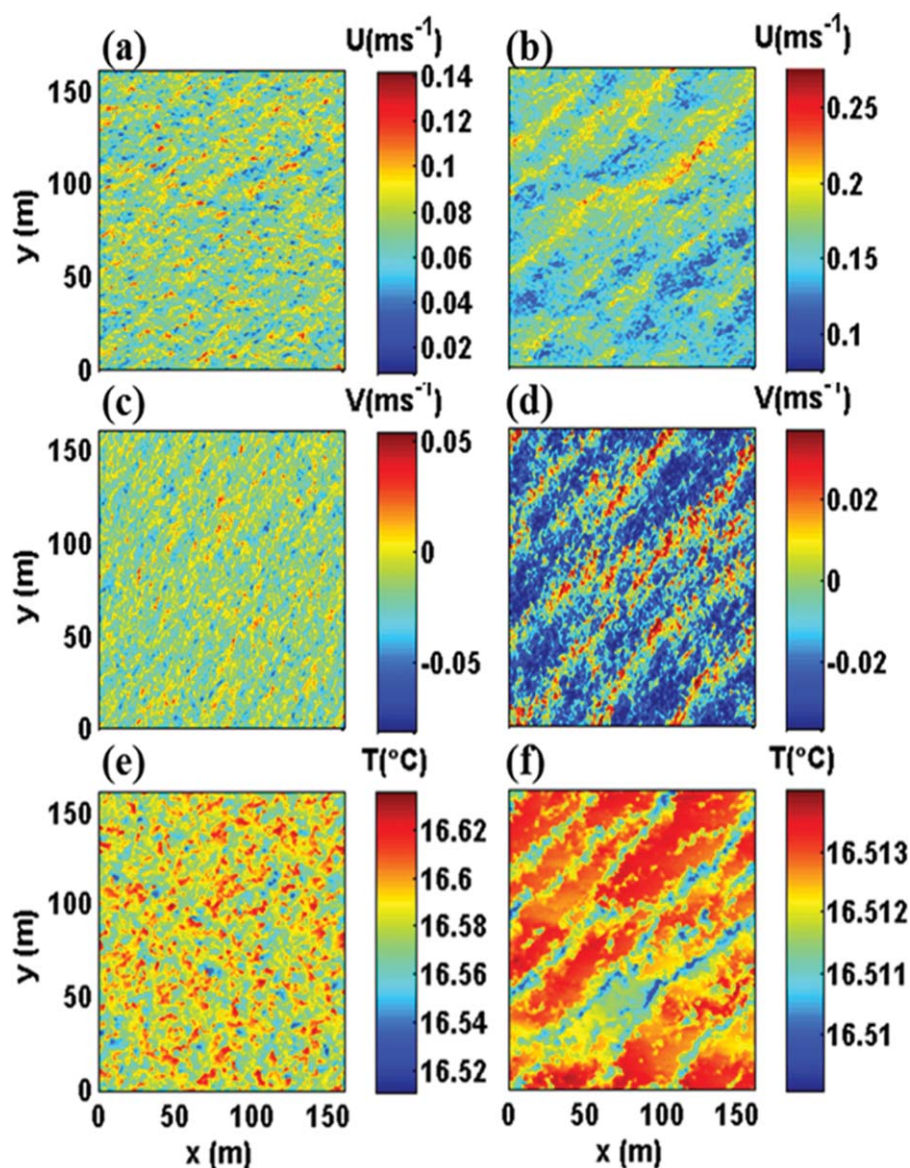


**Figure 6.** Horizontal distributions of (a and b) the east-west velocity, (c and d) the north-south velocity, and (e and f) temperature at hour 12 (left column) and hour 18 (right column) during P1, all at the depth of 3.25 m.

forcing condition, the turbulent flows were disorganized and weak. Under the condition of high winds and large waves, the flows organized into bands parallel to the wind direction. The streaky structures are evident in the plots of horizontal velocity components and temperature.

[23] After examining the turbulent flows and temperature structures at two times in detail, we now look at the diurnal cycle of the ocean mixed layer at the CBLAST site. In Figure 7, we plot the time-depth distributions of mean (horizontally averaged) temperature and heat flux. The temporal evolution of the mean temperature clearly showed the development of diurnal mixed layer during both days. However, there were striking differences between October 8 and 9. The diurnal mixed layer was terminated by LST 1800 October 8 when strong wind/waves produced strong mixing and vertical heat flux that erased the stratification created by the earlier surface heating. On October 9, when

the vertical heat flux was weak due to weak wind and waves, significant stratification developed in the top 5 m and persisted longer.

[24] To illustrate how the turbulence field evolved with time, we plot the time series of horizontally averaged TKE and energy dissipation rate ( $\epsilon$ ) at two depths: 0.75 m affected by breaking waves and 3.75 m affected by turbulent large eddies (Figures 7c and 7d). Unsurprisingly, the TKE maxima occurred during high wind events. The patterns were similar at both depths, but the magnitude of variability was larger closer to the surface than at the deeper depth. The energy dissipation rates at the two depths tell a similar story: dissipation is larger during wind events and smaller during times of weaker wind forcing. The dissipation rate at the near-surface location is larger than the dissipation rate at the deeper location. During the time of weak winds and strong

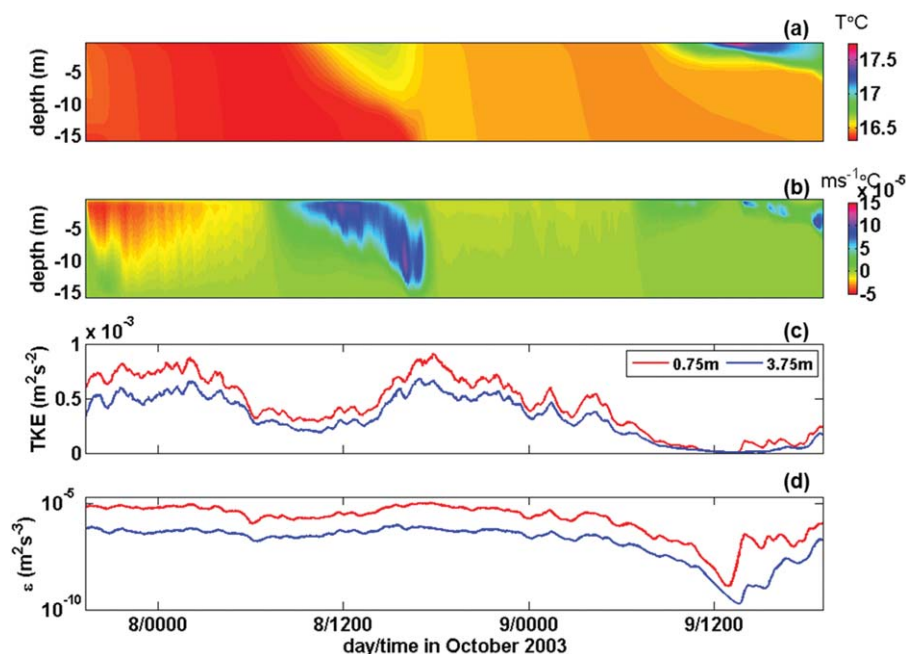


**Figure 7.** Time-depth distributions of horizontally averaged temperature ( $^{\circ}\text{C}$ ) (a) and heat flux ( $^{\circ}\text{C ms}^{-1}$ ) (b); time series of TKE (c); and dissipation rate (d) at the depths of 0.75 m (red) and 3.25 m (blue) during P1. TKE is shown using a linear scale, and dissipation rate is shown using a logarithmic scale.

solar heating (around noon on 9 October), the TKE and dissipation rates were extremely small.

[25] Daytime heating may lead to strong stratification, which can suppress the vertical scale of turbulent large eddies. This eddy size is characterized by the Ozmidov scale [Dillon, 1982]. A question is raised whether the LES model can resolve the energy containing eddies under the strong heating. In Figure 8, we compare the model's vertical grid size  $\Delta z$  against the Ozmidov length scale  $L_o = (\varepsilon/N^3)^{1/2}$  where  $\varepsilon$  is the energy dissipation rate and  $N$  is the buoyancy frequency. The grid size is smaller than the turbulent length scale  $L_o$  throughout the water column, during both the night-time cooling and day-time heating.

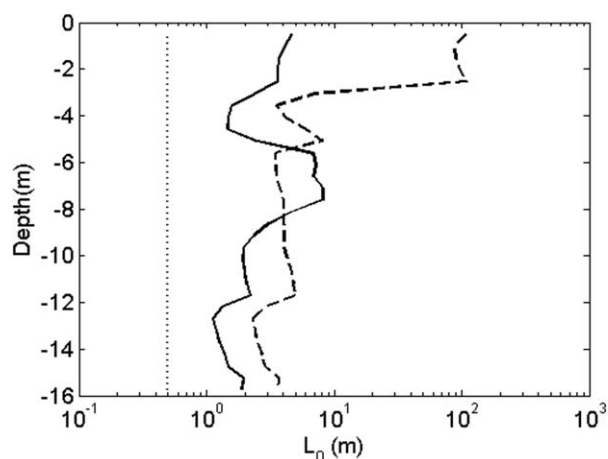


**Figure 8.** Comparison of Ozmidov length scale  $L_o$  at noon (solid) and midnight (dashed). The vertical grid size is shown as the dotted line.

Hence, the LES model can resolve the turbulent large eddies over the range of stratification conditions encountered during the CBLAST-low experiment.

### 3.2. Model-Data Comparison

[26] We have shown the LES simulation of the upper-ocean response to the wind and wave forcing during a 2 day period. In the following sections, we compare several quantities in all five LES numerical experiments and CBLAST observations: vertical velocity variance, TKE, energy dissipation rate, and heat flux. During the CBLAST experiment, velocity measurements were made by six Sontek 5-MHz Ocean Probe acoustic Doppler velocimeters (ADV) deployed at 1.7 and 2.2 m below the mean sea surface. High-frequency temperature measurements were made with fast-response thermistors located within the ADV sample volumes. Gerbi *et al.* [2009] used a spectral fitting approach to estimate turbulent velocity variances in each direction, TKE and energy dissipation rate.

[27] Vertical velocity variance  $\sigma_w^2/u_*^2$  is one useful metric to characterize turbulent large eddies in the upper ocean. Previous observations in the ocean [e.g., D'Asaro, 2001; Tseng and D'Asaro, 2004] and modeling investigations of Langmuir turbulence [e.g., McWilliams *et al.*, 1997; Li *et al.*, 2005] have shown that the vertical velocity variance normalized by the square of the friction velocity is 2–3 times larger than that in shear turbulence. Figure 9a shows a comparison of the modeled  $\sigma_w^2/u_*^2$  against the CBLAST observations. The vertical velocity variance obtained from the LES model is in reasonable agreement with the observations. The normalized  $\sigma_w^2/u_*^2$  varies between 1.5 and 2.5 away from the surface and bottom boundaries. These values are much larger than the range of 0.2–1.0 found for turbulence at a rigid boundary [Hinze, 1975] and are also

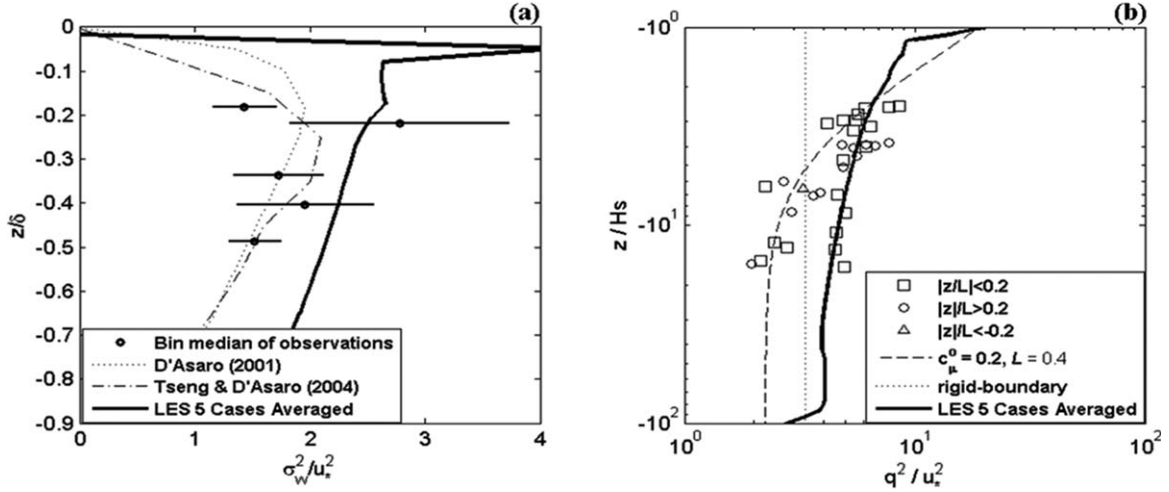


**Figure 9.** (a) Comparison of LES-predicted (solid line) and observed vertical distributions of vertical velocity variances: CBLAST experiment (solid dots with error bars) and autonomous-float measurements from *D'Asaro* [2001] and *Tseng and D'Asaro* [2004] (thin lines). The depth is scaled by the mixed-layer depth or water depth. (b) Comparison of LES-predicted (thick line) and CBLAST-observed (symbols) TKE with that expected from the analytic solutions (dashed line) to the TKE equation by *Craig* [1996] and *Burchard* [2001]. The dotted line represents the solution expected from the rigid-lid boundary theory. As in *Gerbi et al.* [2009], we broke the observational data points into three groups: squares, circles, and triangles, which are characterized by the Monin-Obukhov parameter  $|z|/L < 0.2$  (near neutral),  $> 0.2$  (slightly stable) and  $< -0.2$  (slightly unstable), respectively. The depth is scaled by the significant wave height associated with wind waves.

somewhat larger than the values observed in the open ocean [*D'Asaro*, 2001; *Tseng and D'Asaro*, 2004; *Li et al.*, 2005]. The cause of the surface spike in the modeled  $\sigma_w^2/u_*^2$  is likely due to the parameterization of breaking waves in the LES model.

[28] In Figure 9b, we compare the vertical profile of TKE between the LES model and observations. We normalize the depth by the significant wave height associated with wind waves and TKE by the square of the friction velocity. The LES model agrees well with a majority of the observational data. The normalized TKE  $q^2/u_*^2$  is in the range of 5–8, which are significantly larger than a value of  $\sim 3$  predicted from the rigid-lid theory [*Craig*, 1996; *Burchard*, 2001]. This again shows that wave-driven turbulence rather than shear-driven turbulence dominates at the CBLAST site. However, there are a few data points under stable and neutrally stable conditions that are significantly smaller than the LES model predictions and clustering around a ratio for the rigid-lid boundary value. Those data were collected at times when both the swell and wind waves were small and Stokes forcing may have been minimal.

[29] Energy dissipation rate  $\varepsilon$  is another key turbulence quantity to test the LES model predictions. Similarly to observations in earlier studies [e.g., *Agrawal et al.* 1992; *Terray et al.* 1996; *Drennan et al.* 1996], the dissipation rate in the wave-affected zone was much larger in the CBLAST observations than what would be expected for rigid-boundary turbulence (Figure 10). The observed dissipation rates are predicted reasonably well by the scaling of *Terray et al.* [1996], which follows from assuming that dissipation balances the divergence of downward transport of TKE from the breaking waves [*Craig and Banner*, 1994]. This scaling in the wave-affected zone is written as:

$$\varepsilon = 0.3 \frac{G_t u_*^3 H_s}{z^2} \quad (15)$$

where  $G_t$  is an empirical function of the wave age and  $H_s$  the significant wave height. For the observational data to collapse

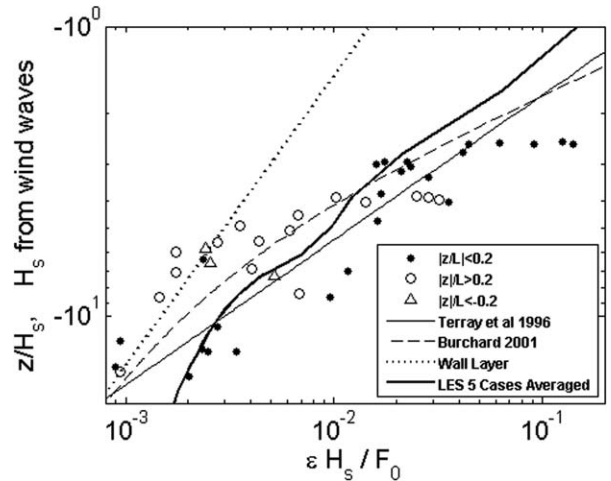


**Figure 10.** Comparison between LES-predicted (thick solid line, 5 case averaged) and observed (symbols) dissipation rate. The thin solid line shows the scaling of *Terray et al.* [1996], the thin dashed line shows the model prediction of *Burchard* [2001] and *Craig* [1996], and the thin dotted line is the expected dissipation rate using neutral rigid-boundary scaling. The symbols indicate different stability regimes, characterized by the Monin-Obukhov parameter. Water depth is normalized by significant wave height while the dissipation rate is normalized as suggested by *Terray et al.* [1996].

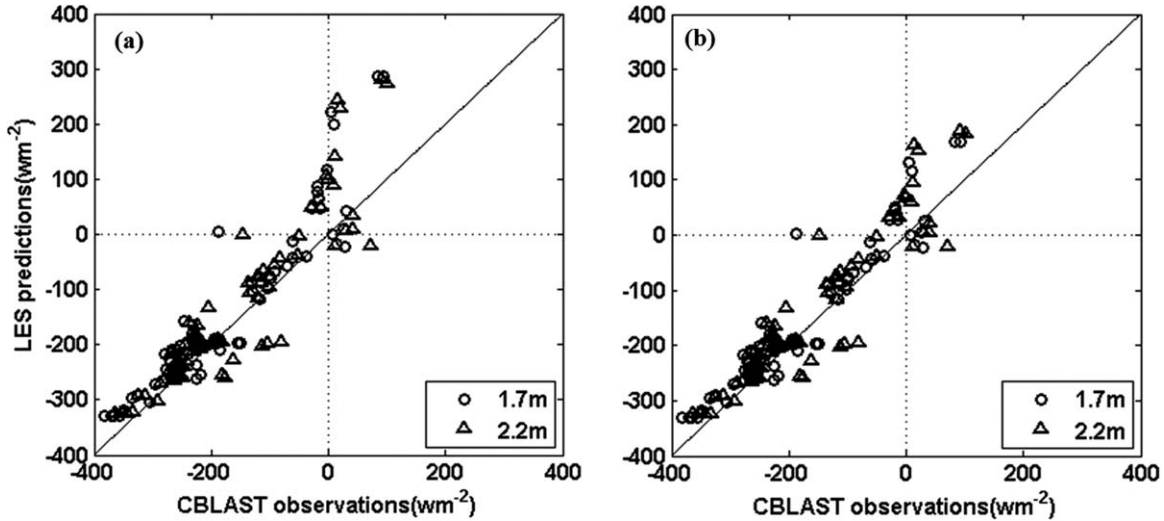


**Figure 11.** Comparison between LES-predicted and CBLAST-observed heat flux at 1.7 m (circle) and 2.2 m (triangle) depths: (a) model estimates; (b) model estimates corrected for penetrative heating.

to this scaling, *Gerbi et al.* [2009] used the significant wave height of the wind waves rather than that of the full spectrum. The dissipation profile for the LES model is obtained from the average over the five LES simulation periods. We compare this profile to the observations, and to shear-driven wall-layer scaling, the scaling of *Terray et al.* [1996], and the model prediction from *Burchard* [2001] who considered wave breaking effects. The LES results show reasonable agreement with the observational data, although there is some disagreement with the shallowest observations. The LES results are similar to the predictions of *Terry et al.* [1996] and *Burchard* [2001], suggesting that the LES captured the enhanced dissipation rates in the near-surface wave zone. At depths deeper than 10 times the significant wave height, the dissipation rate in the LES exceeds the prediction for the breaking waves. The dissipation rate decays more slowly with depth than that predicted for breaking waves only.

[30] Next, we compare observational and LES estimates of the vertical flux of heat by turbulence. As with TKE, *Gerbi et al.* [2008] used a spectral fitting technique to estimate heat flux at two depths below the mean sea surface, 1.7 and 2.2 m. Figure 11a compares the LES predictions to the observations. There is good agreement between the model and observations under unstable conditions (negative surface heat fluxes), but the LES model overpredicts the turbulent heat flux under stable conditions. This is likely due to the way that solar radiation was handled in the LES. All the incoming shortwave energy was added to the top grid cell and none was allowed to penetrate as radiation. Therefore, the model transports heat downward via turbulence rather than allowing downward transport by penetrating radiation. In the heat flux comparison, to correct for the vertical heat transport that should have been accomplished by radiation, we estimate the radiative portion and estimated using,

$$\frac{Q_r}{Q_0} = Re^{z/\zeta_1} + (1 - R)e^{z/\zeta_2} \quad (16)$$

where  $Q_r$  is the shortwave heat flux at depth  $z$ , and  $Q_0$  is the shortwave heat flux at the surface [*Paulson and Simpson*

1977]. For type III water,  $R = 0.78$ ,  $\zeta_1 = 1.4$  m,  $\zeta_2 = 7.9$  m, approximately 36% of the solar radiation passes the measurement depth of 2 m. Subtracting this from the LES estimate of the heat flux, we obtain a new model estimate that is in better agreement with the observational estimate (Figure 11b).

## 4. Discussions

[31] Given the general agreement between the LES model results and turbulence observations, we now address the question on the roles of breaking waves and Langmuir circulation in turbulence dynamics. Recent idealized LES modeling investigations by *McWilliams et al.* [2012] have shown that in the presence of wave breaking and Stokes drift at steady state, the dominant terms in the TKE budget are injection by breaking waves, transport divergence, and dissipation, with a secondary role played by Stoke shear production. The CBLAST observations of *Gerbi et al.* [2009] show similar results, although they were unable to directly measure all terms in the budget. They found that dissipation rates were larger than buoyancy production/damping, Stokes production, shear production, and the rate of change of TKE. The unmeasured terms are transport divergence and direct injection of TKE by breaking waves [see *McWilliams et al.*, 2012]. They concluded that below the region of direct energy injection, the energy dissipation is primarily balanced by the divergence of TKE flux generated by the breaking waves. We now re-examine the TKE budget balance using the LES simulations of the CBLAST observational periods.

### 4.1. TKE Budget Analysis

[32] The horizontally averaged TKE equation can be written as [e.g., *Skylingstad et al.*, 2000]:

$$\begin{aligned} \frac{\partial \bar{E}}{\partial t} = & -\overline{u'_i u'_3} \frac{\partial U_i}{\partial x_3} - \overline{u'_i u'_3} \frac{\partial U_s}{\partial x_3} - \overline{u'_3 g' \rho'} + \frac{\partial}{\partial x_3} \left( \overline{u'_3 p'} \right) \\ & - \frac{\partial}{\partial x_3} \left( \overline{u'_3 E} \right) - \langle \varepsilon \rangle + \text{SGS} \end{aligned} \quad (17)$$

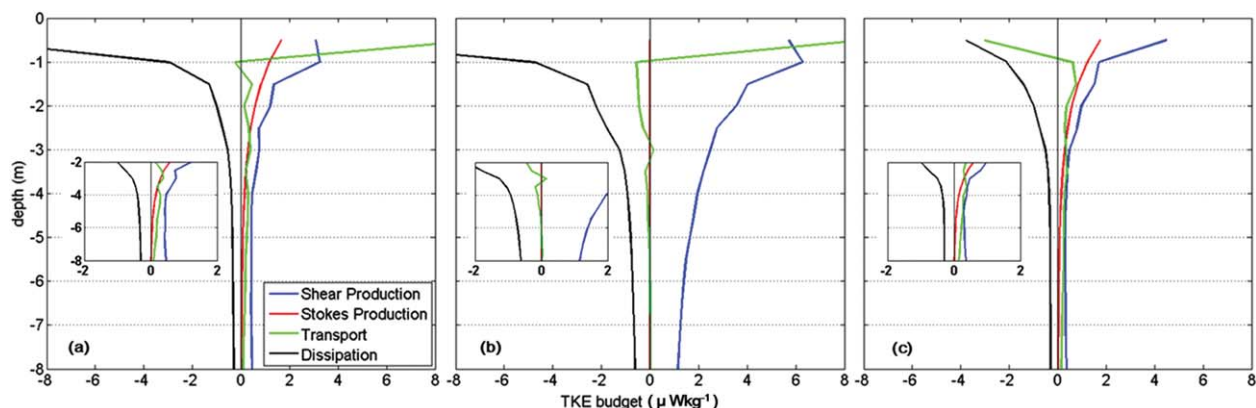


**Figure 12.** Comparison of TKE budget terms among three LES runs: (a) wave breaking and Langmuir circulation; (b) wave breaking only; and (c) Langmuir circulation only. The budget terms are calculated from 2 h averages around hour 18 in P1. The inserts show zoomed-in views of TKE terms in depths of 2–8 m.

where  $\bar{E} = \frac{1}{2}(\overline{u^2 + v^2 + w^2})$  is the TKE, and the terms on the right-hand side of equation (17) are the shear production, Stokes production, buoyancy production, pressure and turbulence transports, and dissipation. SGS represents all other unresolved subgrid scale terms [except for  $\epsilon$ , *Skyllingstad et al., 2000*].

[33] We analyze the TKE budget for a 2 hour period (hours 17–19) during Event P1 where the wind and wave forcing were relatively constant. Figure 12a shows the vertical profiles of four major TKE budget terms: turbulent transport, Stokes production, shear production, and dissipation. Other terms such as time tendency, buoyancy production, and SGS are smaller and add up to close the TKE budget balance but are not plotted. The dominant balance in the upper meter is between turbulent transport and dissipation. At deeper depths, the shear production is the primary term that balances dissipation. The Stokes production is smaller than the shear production, and it decreases exponentially with depth due to the rapid decay of the Stokes drift current. At deep depths, the transport term is about 1/3 to 1/2 of the shear production term.

[34] To discern the separate roles of breaking waves and Langmuir circulation, we have examined two additional model configurations: one with wave breaking but no Stokes drift and one with Stokes drift but no wave breaking. Figures 12b and 12c show the TKE budget terms averaged over the same 2 hour period for these two simulations. In the case with wave breaking only, the dominant TKE budget balance is between TKE transport and dissipation in the near-surface zone and between shear production and dissipation at deeper depths. Such near-surface TKE balance was also found in idealized LES simulations of the upper ocean [Noh et al., 2004; McWilliams et al., 2012]. In the case with Stokes drift only, near the surface, the shear production and Stokes production act as sources for TKE and the transport divergence acts as a sink, carrying TKE to deeper depths where it is dissipated. At deeper depths, the shear production, transport divergence, and the Stokes production all contribute to balancing dissipation. These results are somewhat different from those found by Kukulka et al. [2012]. At depths greater than 2 m, they found that the transport divergence is a leading order term.

The Stokes production decays with depth as in our model, but the shear production becomes small and slightly negative. In both of our model runs with Stokes drift (Figures 12a and 12c), the shear production is larger than the transport term, although it is still much smaller than the shear production in the model run with wave breaking only (Figure 12b). We suspect that many of the differences between our results and those of Kukulka et al. [2012] are caused by the Coriolis force that was included in our simulations but not in those of Kukulka et al. [2012].

[35] The combined effects of wave breaking and Langmuir circulation are well illustrated in the TKE budget comparisons. The TKE budget is dominated by a balance between the TKE transport and dissipation in the near-surface layer, indicating that wave breaking is a dominant source of TKE near the surface. Although most of the breaking wave energy is dissipated near the sea surface, a small portion of it is transported downward. Below the near-surface layer, the TKE transport term is of the similar magnitude in the two LES runs with Stokes drift forcing. This suggests that Langmuir circulation as shown in Figures 5 and 6 may play a significant role in distributing near-surface TKE downward. This result is in general agreement with the idealized LES studies by McWilliams et al. [2012]. They found that wave-breaker energy injection and Stokes production are primary sources of TKE in the wave-affected surface layer, while the turbulent transport plays an important role in transporting TKE downward in the rest of Ekman layer.

[36] Table 1 compares the averages from all the available and usable data collected during the CBLAST experiment (at a depth of  $\sim 2$  m) against the averages obtained from the five representative LES experiments. We note that the averages in the table represent the full-time periods in each simulation that lasted between 5 and 48 h. In contrast, Figure 12 averages over a 2 h period of strong wind forcing in the P1 simulation. There is general consistency between the observational and model estimates. The dissipation has a magnitude of  $O(10^{-6}) \text{ m}^2\text{s}^{-3}$ . The turbulent transport is of the similar magnitude and is the largest term balancing the turbulent dissipation. The shear production has an order of magnitude of  $O(10^{-7}) \text{ m}^2\text{s}^{-3}$ . Averaged over each

**Table 1.** Terms (in Units of  $\text{m}^2 \text{s}^{-3}$ ) in the Turbulence Kinetic Energy Budget for All CBLAST Observations and Averages for Each Individual Period in the Simulations<sup>a</sup>

Exp.		Dissipation ( $\times 10^{-6}$ )	Transport ( $\times 10^{-6}$ )	Shear Production ( $\times 10^{-7}$ )	Stokes Production ( $\times 10^{-8}$ )	Buoyancy ( $\times 10^{-8}$ )
Observation (CBLAST)		1.83	(1.17)	6.11 (max)	0.5	4.70
LES (P1)	2.25 m	0.89	1.25	0.27	1.04	7.37
	1.75 m	1.09	1.51	0.80	1.40	7.50
LES (P2)	2.25 m	0.36	0.50	0.34	0.01	2.51
	1.75 m	0.41	0.60	0.37	0.02	2.52
LES (P3)	2.25 m	0.37	0.41	0.35	0.18	4.81
	1.75 m	0.21	0.24	0.67	0.32	4.21
LES (P4)	2.25 m	1.41	1.54	4.97	0.21	11.50
	1.75 m	1.83	2.02	5.80	0.34	11.50
LES (P5)	2.25 m	0.66	0.66	1.59	2.60	4.69
	1.75 m	0.53	0.86	1.58	4.00	4.73

<sup>a</sup>Averages in the LES results were taken from depths of 1.75 and 2.25 m.

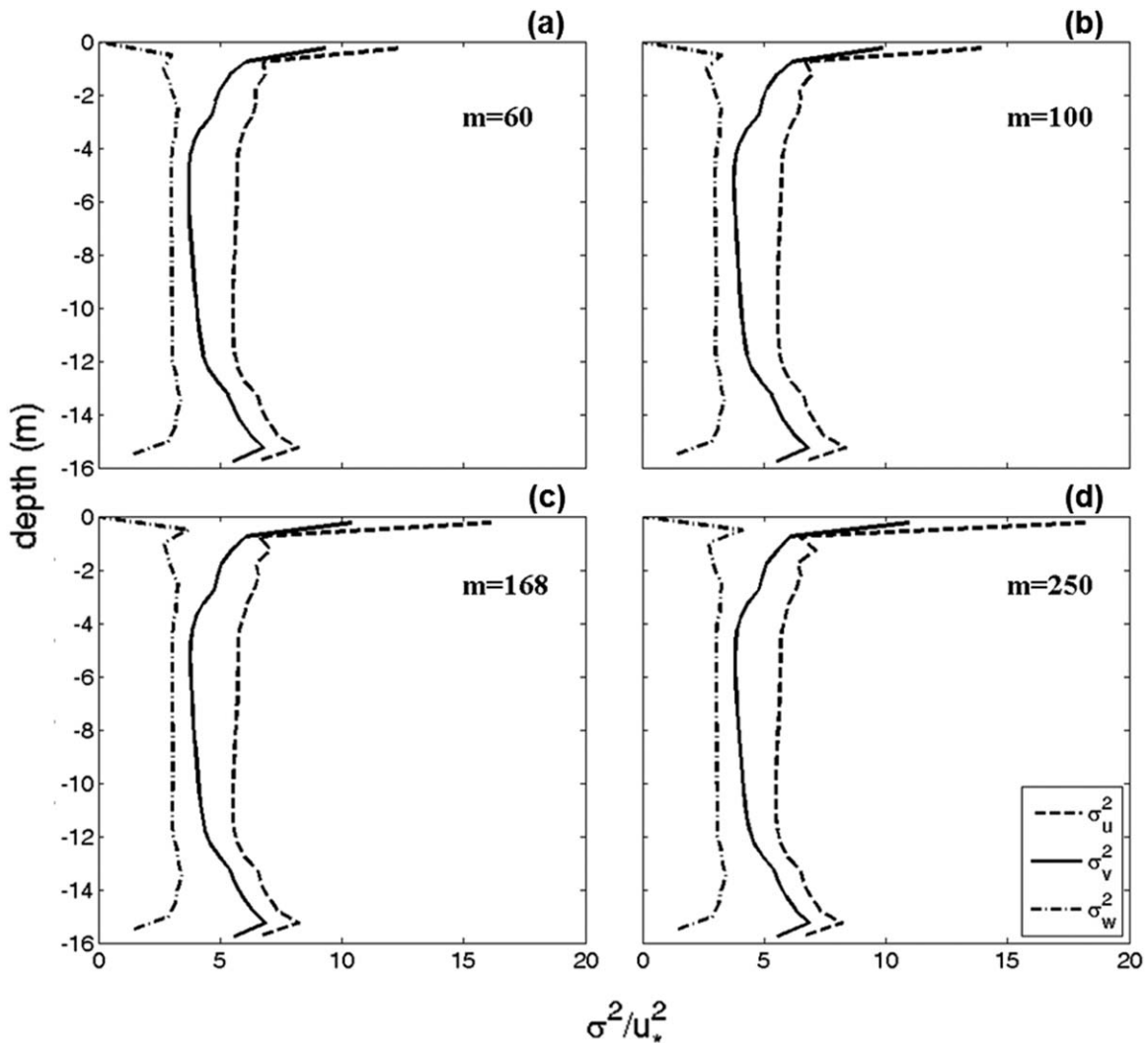


**Figure 13.** Comparison of vertical profiles of turbulence intensities from the LES experiment P4 with the wave-breaking factor  $m = 60$  (a), 100 (b), 168 (c), and 250 (d): the dashed lines correspond to turbulence intensity in the east-west direction; the solid lines in the south-north direction, and the dash-dot lines in the vertical direction.

simulated time period, both Stokes production and buoyancy production are 1–2 orders of magnitude smaller than the dissipation rate. In the LES models, divergence of transport is the primary source of TKE in the wave-affected layer. This is consistent with the observations in which the shear production, Stokes production, and buoyancy production terms did not balance the observed dissipation rates.

#### 4.2. Sensitivity to $m$ Values in Wave-Breaking Parameterization

[37] To represent the effects of wave breaking in the LES model, *Noh et al.* [2004] introduced small-scale random velocity fluctuations at the sea surface whose velocity ( $\alpha u_*$ ) and length scales ( $l_0$ ) are consistent with observations in the ocean. *Noh et al.* [2004] adjusted the velocity scale (i.e.,  $\alpha = 6.57$ ) such that the profile of the resultant dissipation rate is consistent with the observed one [*Agrawal et al.*, 1992; *Craig and Banner*, 1994; *Terray et al.*, 1996]. The equivalent energy flux due to breaking waves is  $I = mu_*^3$  with  $m \approx 40$ . This is lower than the value ( $m=100$ ) suggested in the turbulence closure model of *Craig and Banner* [1994], while *Gerbi et al.* [2009] used  $m = 168$  for the analysis of turbulence statistics obtained from CBLAST observations. Conceivably, the coefficient  $m$  varies with the sea state and wave age: with reported ranges of observational estimates of  $40 < m < 250$  [*Agrawal et al.*, 1992; *Craig and Banner*, 1994; *Drennan et al.*, 1996; *Terray et al.*, 1996; *Feddersen et al.*, 2007], but a preliminary examination on the connection between wave-induced momentum flux and wave age did not yield a simple relationship or equation (*J. Gemmrich*, personal communication, 2012).

[38] In order to examine the sensitivity of the LES model results to changes in  $m$ , we conducted four simulations for different values of  $\alpha$  or  $m=60, 100, 168$ , and 250. We selected Event P1 for this sensitivity analysis, but the results are similar for the other events. Figure 13 compares the vertical profiles of the vertical and two horizontal velocity variances among the four runs. There are significant differences in the top grid cell: larger  $m$  values lead to larger turbulence intensities. However, the turbulence intensities are remarkably similar below the near-surface layer. Larger surface TKE flux produces stronger energy dissipation and higher energy cycle throughput rates but does not greatly increase turbulent intensities. A similar decoupling between TKE and the energy input due to breaking waves was found by *McWilliams et al.* [2012]. Therefore, the LES model parameterization of wave breaking is not sensitive to choices of  $m$  within the observed range.

## 5. Conclusion

[39] We have used the Large Eddy Simulation (LES) model to conduct hindcast simulations of the CBLAST observations that were collected at the Martha's Vineyard Coastal Observatory's Air-Sea Interaction Tower during the CBLAST experiment in 2003. The LES predictions for the vertical velocity variance, TKE, energy dissipation rates, and heat flux are in reasonable agreement with the near-surface turbulence measurements collected during CBLAST. It is encouraging to see that some turbulence clo-

sure models that incorporate the effects of wave breaking [e.g., *Burchard*, 2001] produce vertical profiles of TKE and energy dissipation rate in agreement with the observational data and LES simulation results. The three-dimensional model outputs obtained from the LES model could provide another very useful dataset to further refine the turbulence closure models for upper-ocean studies.

[40] Our analysis using the LES results shows a near-surface region dominated by breaking waves, a deeper region dominated by Langmuir circulation, and a possible coupling between the two processes: Langmuir circulation transports undissipated breaking wave energy downward. In the simple model used in this paper, the influence of wave breaking is assumed to be confined to the sea surface and the temporal and spatial variability of wave breaking is represented by an ensemble average. In the future, it would be interesting to extend the stochastic breaker model of *Sullivan et al.* [2007] to do realistic hindcast simulations of the upper-ocean turbulent flows under changing wind and wave-forcing conditions.

[41] **Acknowledgments.** John Trowbridge, Al Plueddemann, Jim Edson, and Gene Terray played essential roles in collecting and analyzing the data used here. We thank Yun Li, Peng Jia, and Hailun He for helpful discussions and two reviewers for their insightful comments. S. Li and J. Song acknowledge support from the National Natural Science Foundation of China (41206015, 41176016), the National Basic Research Program of China (2011CB403501, 2012CB417402), and the Fund for Creative Research Groups by NSFC (41121064). M. Li acknowledges support from Office of Naval Research (grant N00014-02-1-0659). This is UMCES contribution number 4814.

## References

- Agrawal, Y. C., E. A. Terray, M. A. Donelan, P. A. Hwan, A. J. Williams, W. M. Drennan, K. K. Kahma, and S. A. Kitaigorodskii (1992), Enhanced dissipation of kinetic energy beneath surface waves, *Nature*, 359, 219–220.
- Alvelius, K. (1999), Random forcing of three-dimensional homogeneous turbulence, *Phys. Fluids*, 11, 1880–1889.
- Banner, M. L. (1990), Equilibrium spectra of wind waves, *J. Phys. Oceanogr.*, 20, 966–984.
- Belcher, S. E., et al. (2012), A global perspective on Langmuir turbulence in the ocean surface boundary layer, *Geophys. Res. Lett.*, 39, L18605, doi:10.1029/2012GL052932, 2012.
- Black, P. G., et al. (2007), Air–sea exchange in hurricanes: Synthesis of observations from the coupled boundary layer air–sea transfer experiment, *Bull. Am. Meteorol. Soc.*, 88, 357–384.
- Burchard, H. (2001), Simulating the wave-enhanced layer under breaking surface waves with two-equation turbulence models, *J. Phys. Oceanogr.*, 31, 3133–3145.
- Chen, S. S., J. F. Price, W. Zhao, M. A. Donelan, and E. J. Walsh (2007), The CBLAST hurricane program and the next-generation fully coupled atmosphere–wave–ocean models for hurricane research and prediction, *Bull. Am. Meteorol. Soc.*, 88, 311–317.
- Churchill, J. H., A. J. Plueddemann, and S. M. Faluotico (2006), Extracting wind sea and swell from directional wave spectra derived from a bottom-mounted ADCP, *Tech. Rep. 2006–13*, 34 pp., Woods Hole Oceanogr. Inst., Woods Hole, Mass.
- Craig, P. D., and M. L. Banner (1994), Modeling wave-enhanced turbulence in the ocean surface layer, *J. Phys. Oceanogr.*, 24, 2546–2559.
- Craig, P. D. (1996), Velocity profiles and surface roughness under breaking waves, *J. Geophys. Res.*, 101(C1), 1265–1277.
- Craik, A. D. D., and S. Leibovich (1976), A rational model for Langmuir circulations, *J. Fluid Mech.*, 73, 401–426.
- D'Asaro, E. (2001), Turbulent vertical kinetic energy in the ocean mixed layer, *J. Phys. Oceanogr.*, 31, 3530–3537.
- Dillon, T. M. (1982), Vertical overturns: A comparison of Thorpe and Ozmidov length scales, *J. Geophys. Res.*, 87(C12), 9601–9613.

- Donelan, M. A., F. W. Dobson, S. D. Smith, and R. J. Anderson (1993), On the dependence of sea surface roughness on wave development, *J. Phys. Oceanogr.*, **23**, 2143–2149.
- Drennan, W. M., M. A. Donelan, E. A. Terray, and K. B. Katsaros (1996), Oceanic turbulence measurements in SWADE, *J. Phys. Oceanogr.*, **26**, 808–815.
- Ducros, F., P. Comte, and M. Lesieur (1996), Large-eddy simulation of transition to turbulence in a boundary layer developing spatially over a flat plate, *J. Fluid Mech.*, **326**, 1–36.
- Edson, J. B., et al. (2007), The coupled boundary layers and air-sea transfer experiment in low winds, *Bull. Am. Meteorol. Soc.*, **88**, 341–356.
- Fairall, C., E. Bradley, J. Hare, A. Grachev, and J. Edson (2003), Bulk parameterizations of air-sea fluxes: Updates and verification for the COARE algorithm, *J. Climate*, **16**, 571–591.
- Feddersen, F., J. H. Trowbridge, and A. J. Williams III (2007), Vertical structure of dissipation in the nearshore, *J. Phys. Oceanogr.*, **37**, 1764–1777.
- Gargett, A. E., J. Wells, A. E. Tejada-Martinez, and C. E. Grosch (2004), Langmuir supercells: A mechanism for sediment resuspension and transport in shallow seas, *Science*, **306**, 1925–1928.
- Gargett, A. E., and J. R. Wells (2007), Langmuir turbulence in shallow water. Part I. Observations, *J. Fluid Mech.*, **576**, 27–61.
- Garrett, J. R. (1997), Review of drag coefficients over the oceans and continents, *Mon. Weather Rev.*, **105**, 915–929.
- Gerbi, P. G., J. H. Trowbridge, A. J. Plueddemann, E. A. Terry, and J. J. Fredericks (2008), Measurements of momentum and heat transfer across the air-sea interface, *J. Phys. Oceanogr.*, **38**, 1054–1072.
- Gerbi, P. G., J. H. Trowbridge, E. A. Terry, A. J. Plueddemann, and T. Kukulka (2009), Observations of turbulence in the ocean surface boundary layer: Energetic and transport, *J. Phys. Oceanogr.*, **39**, 1077–1096.
- Grant, A. L. M., and S. E. Belcher (2009), Characteristics of Langmuir turbulence in the ocean mixed layer, *J. Phys. Oceanogr.*, **39**, 1871–1887.
- He, R., and J. L. Wilkin (2006), Barotropic tides on the southeast New England shelf: A view from a hybrid data assimilative modeling approach, *J. Geophys. Res.*, **111**, C08002, doi:10.1029/2005JC003254.
- Hinze, J.O. (1975), *Turbulence*, 2nd ed., 790 pp., McGraw-Hill, New York.
- Huang, N. E. (1971), Derivation of Stokes drift for a deep-water random gravity wave field, *Deep Sea Res. Oceanogr. Abstr.*, **18**, 255–259.
- Kenyon, K. E. (1969), Stokes drift for random gravity waves, *J. Geophys. Res.*, **74**, 6991–6994.
- Kukulka, T., A. J. Plueddemann, J. H. Trowbridge, and P. P. Sullivan (2009), Significance of Langmuir circulation in upper ocean mixing: Comparison of observations and simulations, *Geophys. Res. Lett.*, **36**, L10603, doi:10.1029/2009GL037620.
- Kukulka, T., A. J. Plueddemann, J. H. Trowbridge, and P. P. Sullivan (2010), Rapid mixed layer deepening by the combination of Langmuir and shear instabilities – A case study, *J. Phys. Oceanogr.*, **40**(11), 2381–2400.
- Kukulka, T., A. J. Plueddemann, J. H. Trowbridge, and P. P. Sullivan (2011), The influence of crosswind tidal currents on Langmuir circulation in a shallow ocean, *J. Geophys. Res.*, **116**, C08005, doi:10.1029/2011JC006971.
- Kukulka, T., A. J. Plueddemann, and P. P. Sullivan (2012), Nonlocal transport due to Langmuir circulation in a coastal ocean, *J. Geophys. Res.*, **117**, C12007, doi:10.1029/2012JC008340.
- Li, M., and C. Garrett (1993), Cell merging and jet/downwelling ratio in Langmuir circulation, *J. Mar. Res.*, **51**, 737–769.
- Li, M., and C. Garrett (1995), Is Langmuir circulation driven by surface waves or surface cooling? *J. Phys. Oceanogr.*, **25**, 64–76.
- Li, M., C. Garrett, and E. Skillingstad (2005), A regime diagram for classifying turbulent large eddies in the upper ocean, *Deep Sea Res., Part I*, **52**, 259–278.
- Li, M., J. Trowbridge, and W. R. Geyer (2008), Asymmetric tidal mixing due to the horizontal density gradient, *J. Phys. Oceanogr.*, **38**, 418–434.
- Li, M., S. Vagle, and D. M. Farmer (2009), Large eddy simulations of upper-ocean response to a midlatitude storm and comparison with observations, *J. Phys. Oceanogr.*, **39**, 2295–2309.
- Li, M., S. Radhakrishnan, U. Piomelli, and W. R. Geyer (2010), Large-eddy simulation of the tidal-cycle variations of an estuarine boundary layer, *J. Geophys. Res.*, **115**, C08003, doi:10.1029/2009JC005702.
- McWilliams, J. C., P. P. Sullivan, and C. H. Moeng (1997), Langmuir turbulence in the ocean, *J. Fluid Mech.*, **334**, 1–30.
- McWilliams, J. C., E. Huckle, J. H. Liang, and P. P. Sullivan (2012), The wavy Ekman layer: Langmuir circulations, breaking waves, and Reynolds stress, *J. Phys. Oceanogr.*, **42**, 1793–1816, doi:10.1175/JPO-D-12-07.1.
- Melville, W. K., and P. Matusov (2002), Distribution of breaking waves at the ocean surface, *Nature*, **417**, 58–63.
- Melville, W. K., F. Veron, and C. J. White (2002), The velocity field under breaking waves: Coherent structures and turbulence, *J. Fluid Mech.*, **454**, 203–233.
- Min, H. S., and Y. Noh (2004), Influence of the surface heating on Langmuir circulation, *J. Phys. Oceanogr.*, **34**, 2630–2641.
- Moeng, C.-H. (1984), A large-eddy simulation model for the study of planetary boundary-layer turbulence, *J. Atmos. Sci.*, **46**, 2311–2330.
- Nimmo-Smith, W. A. M., S. A. Thorpe, and A. Graham (1999), Surface effects of bottom-generated turbulence in a shallow sea, *Nature*, **400**, 251–254.
- Noh, Y., H. S. Min, and S. Raasch (2004), Large eddy simulation of the ocean mixed layer: The effects of wave breaking and Langmuir circulation, *J. Phys. Oceanogr.*, **34**, 720–735.
- Noh, Y., G. Goh, and S. Raasch (2011), Influence of Langmuir circulation on the deepening of the wind-mixed layer, *J. Phys. Oceanogr.*, **41**, 472–484, doi:10.1175/2010JPO-4494.1.
- Paulson, C. A., and J. J. Simpson (1977), Irradiance measurements in the upper ocean, *J. Phys. Oceanogr.*, **7**, 952–956.
- Piomelli, U., and E. Balaras (2002), Wall-layer models for large-eddy simulation, *Annu. Rev. Fluid Mech.*, **34**, 349–374.
- Skyllingstad, E. D., and D. W. Denbo (1995), An ocean large-eddy simulation of Langmuir circulations and convection in the surface mixed-layer, *J. Geophys. Res.*, **100**(C5), 8501–8522.
- Skyllingstad, E. D., W. D. Smyth, J. N. Moum, and H. Wijesekera (1999), Upper-ocean turbulence during a westerly wind burst: A comparison of large-eddy simulation results and microstructure measurements, *J. Phys. Oceanogr.*, **29**, 5–28.
- Skyllingstad, E. D., W. D. Smyth, and G. Crawford (2000), Resonant wind-driven mixing in the ocean boundary layer, *J. Phys. Oceanogr.*, **30**, 1866–1890.
- Smyth, W. D., E. D. Skillingstad, G. B. Crawford, and H. Wijesekera (2002), Nonlocal fluxes and Stokes drift effects in the K-profile parameterization, *Ocean Dyn.*, **52**, 104–115.
- Sullivan, P. P., J. C. McWilliams, and W. K. Melville (2007), Surface gravity wave effects in the oceanic boundary layer: Large-eddy simulation with vortex force and stochastic breakers, *J. Fluid Mech.*, **593**, 405–452.
- Sullivan, P. P., L. Romero, J. C. McWilliams, and W. K. Melville (2012), Transient evolution of Langmuir turbulence in the ocean boundary layers driven by hurricane winds and waves, *J. Phys. Oceanogr.*, **42**, 1959–1979, doi:10.1175/JPO-D-12-025.1.
- Teixeira, M. A. C., and S. E. Belcher (2002), On the distortion of turbulence by a progressive surface wave, *J. Fluid Mech.*, **458**, 229–267.
- Tejada-Martinez, A. E., and C. E. Grosch (2007), Langmuir turbulence in shallow water: Part II. Large-eddy simulations, *J. Fluid Mech.*, **576**, 63–108.
- Tejada-Martinez, A. E., C. E. Grosch, N. Sinha, C. Akan, and G. Martinat (2012), Disruption of the bottom log layer in large-eddy simulations of full-depth Langmuir circulation, *J. Fluid Mech.*, **699**, 79–93.
- Terray, E. A., M. A. Donelan, Y. C. Agrawal, W. M. Drennan, K. K. Kahma, A. J. Williams III, P. A. Hwang, and S. A. Kitaigorodskii (1996), Estimates of kinetic energy dissipation under breaking waves, *J. Phys. Oceanogr.*, **26**, 792–807.
- Thorpe, S. A. (2004), Langmuir circulation, *Annu. Rev. Fluid Mech.*, **36**, 55–77.
- Tseng, R. S., and E. D'Asaro (2004), Measurements of turbulent vertical kinetic energy in the ocean mixed layer from Lagrangian floats, *J. Phys. Oceanogr.*, **34**, 1984–1990.